

Arrested Dynamics of Droplet Spreading on Ice


Venkata Yashasvi Lolla^{1,*}, S. Farzad Ahmadi^{1,2,*}, Hyunggon Park^{1,3,*},

Andrew P. Fugaro^{3,*} and Jonathan B. Boreyko^{1,†}

¹*Department of Mechanical Engineering, Virginia Tech, Blacksburg, Virginia 24061, USA*

²*Department of Mechanical Engineering, University of California Santa Barbara, Santa Barbara, California 93106, USA*

³*Department of Biomedical Engineering and Mechanics, Virginia Tech, Blacksburg, Virginia 24061, USA*

 (Received 1 October 2021; revised 17 March 2022; accepted 27 June 2022; published 11 August 2022; corrected 28 July 2023)

We investigate the arrested spreading of room temperature droplets impacting flat ice. The use of an icy substrate eliminates the nucleation energy barrier, such that a freeze front can initiate as soon as the droplet's temperature cools down to 0°C. We employ scaling analysis to rationalize distinct regimes of arrested hydrodynamics. For gently deposited droplets, capillary-inertial spreading is halted at the onset of contact line freezing, yielding a 1/7 scaling law for the arrested diameter. At low impact velocities ($We \lesssim 100$), inertial effects result in a 1/2 scaling law. At higher impact velocities ($We > 100$), inertio-viscous spreading can spill over the frozen base of the droplet until its velocity matches that of a kinetic freeze front caused by local undercooling, resulting in a 1/5 scaling law.

DOI: [10.1103/PhysRevLett.129.074502](https://doi.org/10.1103/PhysRevLett.129.074502)

The spreading of a droplet's three-phase contact line after contacting a dry surface exhibits rich and complex dynamics [1,2]. Multiple scaling laws have been discovered that capture the various regimes of contact line spreading [3]. Early-time spreading is capillary-inertial with the diameter following a 1/2 power law with respect to time [4,5], where capillarity rapidly drives spreading due to the sharp curvature about the contact line, while the inertia of the droplet resists deformation [6]. Late-time spreading is visco-capillary in nature; the droplet assumes a spherical-cap shape and the spreading dynamics are governed by viscous effects near the contact line until reaching an equilibrium contact angle [7]. For a droplet gently deposited onto a fully wetting surface, this late-time spreading follows a 1/10 power law known as Tanner's Law [8,9]. At high impact speeds, the hydrodynamics governing the maximal spreading diameter (after which retraction may occur) is a rich combination of inertia, surface tension, and viscous dissipation [10].

When the spreading droplet is on a chilled substrate, one has to also consider its heat transfer with the substrate and the resulting onset and propagation of freezing. The influence of solidification on droplet spreading was initially studied in the context of molten metal droplets impacting a solid substrate [11,12]. With respect to freezing an impacting water droplet, most research utilized a chilled substrate that was dry (i.e., no preexisting frost or ice) [13,14]. When the chilled substrate temperature was above -40°C , freezing did not occur upon water droplet impact due to the energy barrier inherent to nucleating an ice embryo [15]. Chilled substrates that are nonwetting can exploit this energy barrier by rebounding and/or sliding supercooled droplets away before ice nucleation can occur

[16,17]. For substrates chilled beneath -40°C , water droplet freezing can occur immediately and dramatically, resulting in surprising effects such as spontaneous delamination [18]. The nucleation energy barrier can be removed entirely by choosing a solid substrate of the same material as the droplet. For example, a water droplet impacting a sheet of ice, which was recently reported but these works were primarily empirical [19,20]. A follow-up study modeled the thickness of the solidified lamella but not the spreading dynamics [15].

Multiple theories have been developed to rationalize the maximal diameter of a droplet spreading on a chilled substrate, where solidification arrests the advancing contact line [21,22]. Schiaffino and Sonin studied the impact of molten wax on a solid wax substrate and proposed that the advancing contact line became arrested once the contact angle of the solidification front matched that of the droplet [23,24]. Chandra and co-workers characterized the solidification of molten metals and wax droplets on room temperature substrates [25,26]. Tavakoli *et al.* studied the spreading of an alkane droplet on glass, finding that solidification began at the contact line with arrest occurring after a critical volume within the contact line was solidified [27]. Ruiter *et al.* studied hexadecane droplets impacting cold copper and glass substrates, suggesting that the spreading becomes arrested after the contact line reaches a critical supercooled temperature where nonequilibrium freezing can occur [28]. None of these models consider the most natural scenario: water droplets impacting an icy surface.

In this Letter, we develop scaling laws that capture the spreading rate and arrest diameter of water droplets impacting a flat ice sheet. For droplets impacting at low

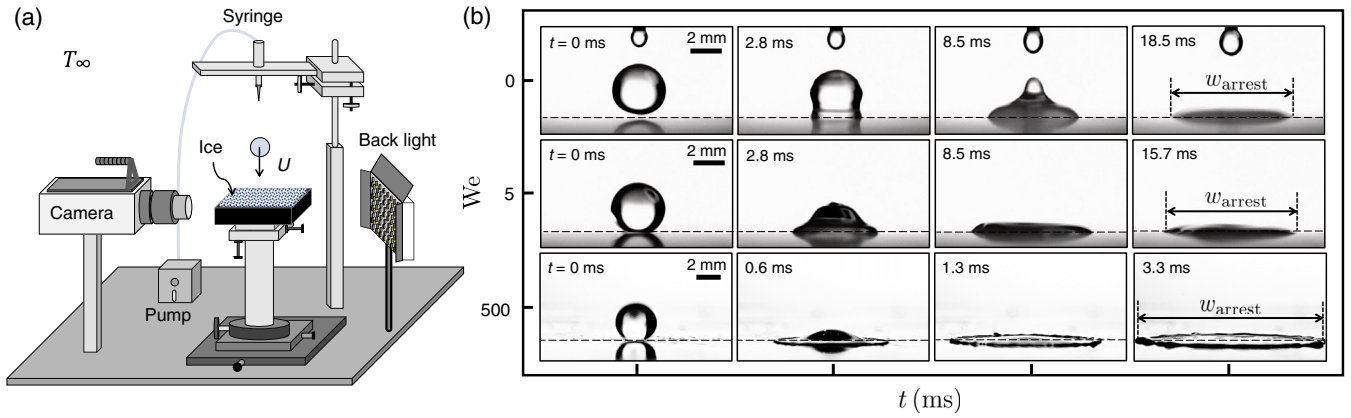


FIG. 1. (a) Schematic of the experimental setup, where room temperature droplets impact a chilled ice substrate. (b) High-speed microscopy of droplet impact and spreading on an ice sheet chilled at $T_s = -20^\circ\text{C}$. For gentle deposition ($We \approx 0$) or impact at relatively low Weber numbers ($We \leq 100$), capillary-inertial spreading became arrested due to the onset of freezing (last frame). When $We > 100$, inertio-viscous spreading is now what becomes arrested.

Weber numbers, the spreading is capillary-inertial and becomes arrested when the droplet cools down to 0°C . At high Weber number impacts, the hydrodynamic spreading quickly transitions from the $1/2$ capillary-inertial power law to a $1/6$ inertio-viscous one with increasing Weber number. The inertial spreading enables local supercooling despite the lack of a nucleation energy barrier, such that arrest occurs once the speed of the nonequilibrium freeze front matches that of the contact line.

Figure 1 depicts the high-speed imaging of water droplets impacting a smooth ice substrate at various Weber numbers: $We = \rho D_0 U^2 / \gamma$, where ρ is the density of water, D_0 is the preimpact droplet diameter, U is the impact velocity, and γ is surface tension. The water droplets were room temperature prior to impact, whereas the ice substrate was varied from $T_s = -30^\circ\text{C}$ to -10°C , see Sec. 2 in the Supplemental Material [29] for more details on the experimental setup. When the water droplet was gently deposited ($We \approx 0$) or released from a small height ($We \approx 5$), the droplet spreading was due to surface tension. The freezing-induced arrest of hydrodynamic spreading (last frame of each row) occurred at $t \approx 18$ ms for the $We \approx 0$ case, but at only $t \approx 15$ ms for $We \approx 5$. Despite the faster arrest time for the latter case, the arrested contact diameter (w_{arrest}) was actually slightly larger due to inertia boosting the capillary spreading. For droplets impacting at $We \approx 500$, inertia causes a rapid spreading but the droplet's hydrodynamic spreading is still curtailed by freezing-induced arrest. In other words, an equivalent droplet impact on a nonfreezing surface would have spread to a larger diameter (followed in some cases by an inertial retraction). The arrest time was only $t \approx 3.5$ ms, but w_{arrest} was nonetheless the largest of the three cases due to the inertial spreading. See Fig. S1 in the Supplemental Material [29] to compare droplet impact on ice to that on dry hydrophilic or superhydrophobic surfaces.

Prior to arrest, spreading follows the well-known capillary-inertial scaling law for a gently deposited droplet ($U \approx 0$ m/s) [4,5],

$$w(t) \sim \beta_1 \left(\frac{\gamma H}{\rho} \right)^{1/4} t^{1/2}, \quad (1)$$

where H is the averaged height of the spreading droplet and $H \sim (D_0)^3 / w^2$ by conservation of mass. Spreading follows an inertial scaling law for droplets impacting the icy substrate ($U > 0$ m/s) [30],

$$w(t) \sim \beta_2 (U D_0 t)^{1/2}, \quad (2)$$

where β_1 and β_2 are numerical prefactors, and t is the time from impact. The best-fit values are $\beta_1 \approx 0.5$, $\beta_2 \approx 10.21$ for $We \approx 5$, and $\beta_2 \approx 5.78$ for $We \approx 100$. While bottom-up imaging is helpful to fully capture early-time droplet spreading [31], this was not possible with our setup and we clearly observed the $1/2$ law nonetheless (Fig. S2). While these $1/2$ spreading laws were originally reported for isothermal conditions, a recent study of hexadecane droplets spreading on a dry, chilled substrate independently validated that they can extend to nonisothermal systems [28]. The slightly slower spreading rates at colder ice temperatures is due to the temperature-dependent increase in viscosity [17]. Here, this effect is secondary, as the use of a preiced substrate causes arrest to occur before the droplet could become supercooled. Technically, spreading always initiates in the inertially limited viscous regime [32,33], but for water the transition to the $1/2$ laws is faster than the temporal resolution of the high-speed camera. The late-time transition to Tanner's $1/10$ power law or partially wetting state was not observed due to the onset of freezing and contact line arrest. See Fig. S3 [29] for the evolution in contact angle during spreading.

Regarding arrest, we hypothesize that the contact line is halted as soon as the droplet's bulk temperature cools down from room temperature to the freezing point (0°C). This is supported by Fig. S4(a) in the Supplemental Material [29], where w_{arrest} decreases with decreasing substrate temperature (T_s), but increases with volume for negligible impact height. The cooling timescale is a balance between the droplet's sensible heat and conduction into the chilled ice,

$$t_{\text{cooling}} \sim \left(\frac{T_l - T_f}{T_l - T_s} \right) \frac{H^2}{\alpha_l}, \quad (3)$$

where $T_l - T_f$ is the differential between the initial liquid temperature and freezing temperature (i.e., sensible cooling required to initiate freezing), $T_l - T_s$ is the initial temperature differential between the droplet and ice that drives the conductive heat transfer, and α_l is the thermal diffusivity of the liquid. Plugging t_{cooling} into Eq. (1) allows for the solution of $w(t_{\text{cooling}}) \sim w_{\text{arrest}}$. Invoking conservation of mass enables H to be substituted out of the equation. Solving for the nondimensional arrest diameter yields

$$\frac{w_{\text{arrest}}}{D_0} \sim \beta_3 \left(\frac{T_l - T_f}{T_l - T_s} \right)^{1/7} \left(\frac{\text{Pr}}{\text{Oh}} \right)^{1/7}, \quad (4)$$

where β_3 is a geometric prefactor that accounts for the crude approximation of a uniform droplet thickness used to derive Eqs. (3) and (4), $\text{Pr} = \nu/\alpha_l$ is the Prandtl number (where $\nu = \mu/\rho$ and μ are the kinematic and dynamic viscosities of water), and $\text{Oh} = \mu/\sqrt{\rho\gamma D_0}$ is the Ohnesorge number. Figure 2 shows that the 1/7 power law from Eq. (4) collapses all of the experimental data over a wide range of volumes; this can alternately be expressed as a 5/14 power law with respect to volume [Fig. S4(b)].

Curiously, this scaling also worked for hexadecane droplets gently deposited on ice [Fig. S4(b)], despite

the chemical mismatch invalidating the model's neglect of a nucleation energy barrier. We attribute this to hexadecane's high freezing temperature (18°C) and low surface tension compared to water, which renders the nucleation energy barrier as approximately negligible. This hypothesis was confirmed by reproducing the 1/7 power law for hexadecane droplets deposited on frozen hexadecane, albeit with more scatter due to the crumpling of the solidifying droplet (Fig. S5 [29]).

For moderate droplet impacts ($5 < \text{We} < 100$, impact height of 1, 2.5, 5, or 10 cm), Eq. (3) would be substituted into Eq. (2) instead of Eq. (1) to account for the inertia of the impacting droplet. The resulting nondimensional arrest diameter now scales as

$$\frac{w_{\text{arrest}}}{D_0} \sim \beta_4 \left(\frac{H}{D_0} \right) \left(\frac{T_l - T_f}{T_l - T_s} \right)^{1/2} (\text{Pr Re})^{1/2}, \quad (5)$$

where β_4 is the geometric prefactor and $\text{Re} = \rho U D_0 / \mu$ is the Reynolds number. The relationship between H and D_0 for high Reynolds numbers (> 1500 for our case) and Weber numbers is given by $H/D_0 \approx \eta/(\tau + \bar{t})^2$ for droplet impacts on dry surfaces [34,35]. Here, $\eta = 0.39$ and $\tau = 0.25$ are empirical constants, whereas $\bar{t} = tU/D_0$ represents the nondimensional timescale and t is the experimental spreading time. Prior to arrest, the impact dynamics on ice follow the same spreading dynamics as that of dry surfaces for moderate impact heights (Fig. S2). Thus, using this relation to our advantage, we obtain values ranging from $H/D_0 = 0.075$ to 0.11. This weak variation is due to capillarity still playing a role for moderate impacts, enabling H/D_0 to get absorbed into the best-fit numerical prefactor [i.e., $\beta_4(H/D_0)$]. Figure 2(b) demonstrates that Eq. (2) collapses all moderate impact data onto a single curve, validating the $(\text{Pr Re})^{1/2}$ power law. For our experiments, $H/D_0 \approx 0.09\text{--}0.3$.

For higher inertial droplet impacts ($\text{We} > 100$, impact heights ≥ 20 cm), the measured spreading rate suddenly

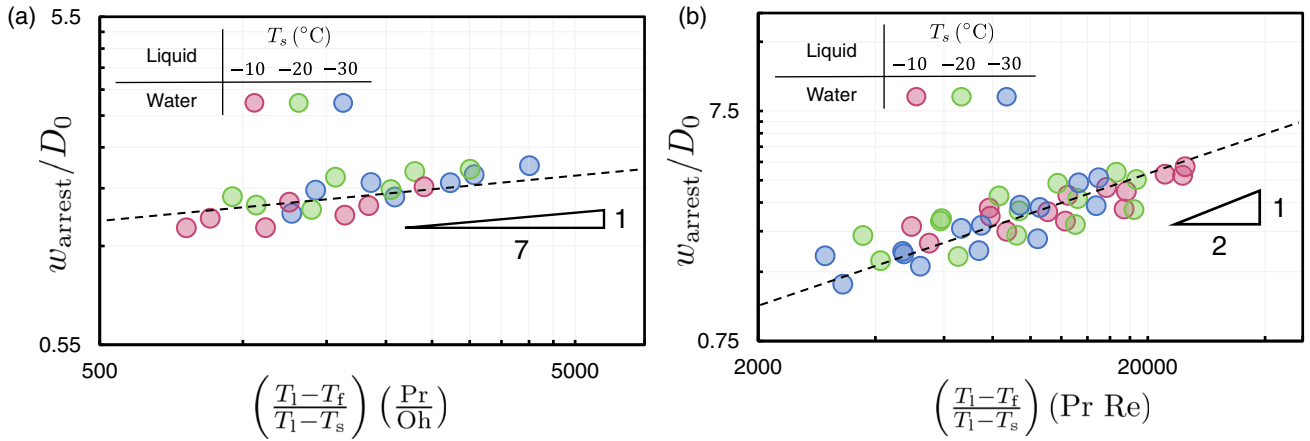


FIG. 2. Nondimensional arrested droplet diameter (w_{arrest}) as a function of nondimensional thermophysical properties of water. (a) Droplets gently deposited on ice follow a 1/7 power law [Eq. (4) with $\beta_3 \approx 0.65$]. (b) Droplets impacting at moderate We numbers follow a 1/2 power law [Eq. (5), where $\beta_4(h/D_0) \approx 0.03$].

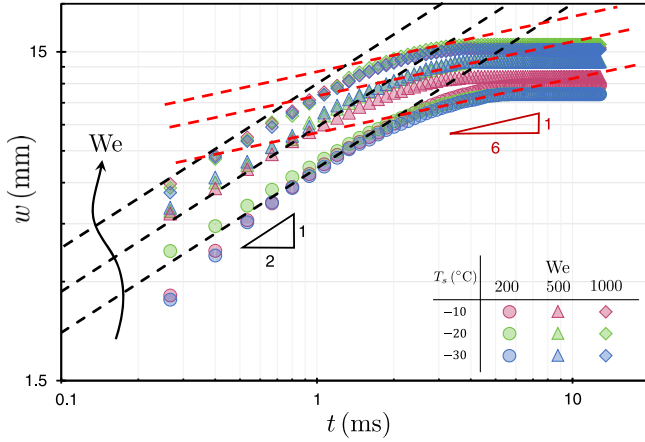


FIG. 3. Evolving spreading radius of water droplets impacting an ice substrate at high Weber numbers ($We > 100$). Dashed black lines correspond to the $1/2$ capillary-inertial spreading law [Eq. (2)], with best-fit values of $\beta_2 \approx 4.8$, 3.7 , and 2.65 for $We = 200$, 500 , and 1000 , respectively. Dashed red lines correspond to the $1/6$ inertio-viscous scaling [Eq. (6)], with $\beta_5 \approx 12.82$, 5.97 , and 0.74 for $We = 200$, 500 , and 1000 , respectively. The subsequent onset of zero slope indicates hydrodynamic arrest.

diverted from the expected power law slope of $1/2$ down to $1/6$. This transition occurred approximately 2 ms after impact and lasted until arrest occurred around $t_{\text{arrest}} \approx 5$ ms (Fig. 3). We hypothesize that, for highly inertial droplet impacts, the $1/6$ regime indicates that the droplet can continue to spread even after its base has frozen. This can be conceptualized as an inertio-viscous regime, where thin-film spillage over the icy base is driven by inertia and resisted by viscous dissipation.

The power law for inertio-viscous spreading is a balance of inertial and viscous stresses: $\rho U^2 \sim \mu(u/H)^2 t$, where u and H are the radial fluid velocity and height of the inertially flattening droplet, respectively. For highly inertial impacts, we assume the viscous effects extend across the entire height of the flattened droplet, such that they matter everywhere. We further assume that the effective radial velocity of the droplet scales with the speed of the advancing contact line: $u \sim w/t$. Finally, incorporating mass conservation, we obtain an expression for the evolving contact diameter,

$$w(t) \sim \beta_5 \text{Re}^{1/6} (UD_0^5)^{1/6} t^{1/6}, \quad (6)$$

where β_5 is a numerical prefactor. Plotting Eq. (6) in Fig. 3, there is an excellent match to the experimental spreading rate over a time range of about $2 \lesssim t \lesssim 5$ ms. The theoretical time where the $1/2$ power law [Eq. (2)] transitions to this $1/6$ power law scales as $t \sim U^{-1} D_0 \text{Re}^{1/2}$, which Fig. 3 shows is also in agreement with the experimental transition (i.e., the theoretical lines intersect where the data suddenly shift in slope). This seemingly validates our hypothesis of

an intermediate inertio-viscous spreading regime before the droplet gets arrested. The $1/6$ scaling also agreed with the results for hexadecane droplets impacting on ice (Fig. S6). While scaling laws of nearly any slope can be misleadingly best fit to transitions between regimes [36], we note that our $1/6$ regime exhibits a nearly constant slope across an appreciable timescale of about 3 ms for multiple liquids. This suggests that the inertio-viscous regime is physical and not a mere crossover between regimes, especially given its derivation from first principles. By plotting the instantaneous power law versus time, it was confirmed that stable $1/2$ and $1/6$ laws occurred for inertial droplet spreading on ice, whereas spreading on room temperature copper only exhibited a stable $1/2$ law (Fig. S7 [29]).

The arrest dynamics for an inertially spreading droplet were distinct from that of the droplets gently spreading by capillarity. For example, the vanishing thickness ($H \rightarrow 0$) of an inertially flattening droplet means that $t_{\text{cooling}} \rightarrow 0$ [Eq. (3)]. Given that the droplet can cool down to a freezing temperature almost immediately, one could naively assume that arrest would occur right away. However, the inertia of the overlying bulk liquid allows for spillage over the frozen contact line, such that w_{arrest} is much larger than what is predicted by the $1/7$ [Eq. (4)] or $1/2$ [Eq. (5)] power laws. We propose that the vanishing thermal resistance of the droplet flattening over the chilled ice, combined with its rapid rate of spreading, results in localized undercooling near the droplet's contact line, despite the lack of a nucleation energy barrier. In other words, the contact line spreads so quickly that it cannot nucleate ice immediately upon reaching 0°C , enabling localized undercooling that then results in nonequilibrium solidification (Fig. S8). This may also explain why the inertia of the pancaking droplet is being resisted by viscous effects rather than by capillarity, both in terms of the increased viscosity of the chilled water and the frozen base inhibiting capillary retraction.

Whereas equilibrium solidification is slow and rate limited by heat transfer (i.e., Stefan problem), nonequilibrium solidification is kinetic in nature. The freeze front velocity, termed the kinetic crystal growth velocity, is related to the extent of undercooling [37,38],

$$v_f = \kappa \Delta T^b, \quad (7)$$

where κ is the kinetic coefficient, $\Delta T = T_f - T_l$ is the extent of liquid undercooling, and b is a nondimensional exponent. The physics of kinetic freezing are complex, such that the numerical values for κ and b are typically chosen to match Eq. (7) with empirical measurements or molecular dynamics simulations [28]. For molten metals, the kinetic coefficient ranged from $\kappa = 0.1$ to $1 \times 10^{-3} \text{ ms}^{-1} \text{ K}^{-1}$, whereas the b term was not considered (i.e., $b = 1$) [28,39,40]. For water impacting a dry, chilled substrate, $\kappa = 2.8 \times 10^{-3} \text{ ms}^{-1} \text{ K}^{-1.8}$ and $b = 1.8$ [37,41].

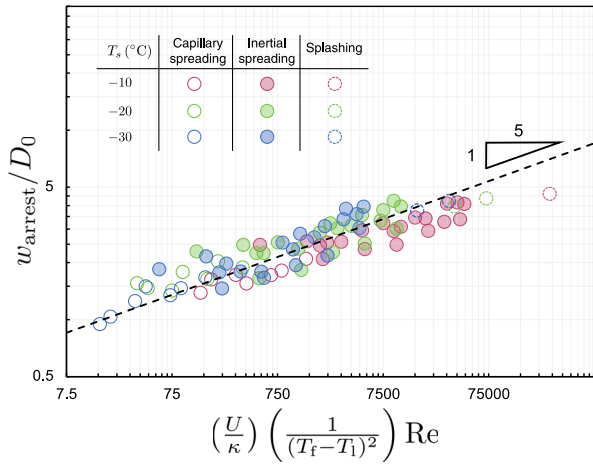


FIG. 4. The nondimensional arrest diameter, where data collapsed onto Eq. (8) (dashed line). Open, filled, and dotted symbols represent the capillary spreading ($We \leq 100$), inertial spreading ($We > 100$), and splashing regimes, respectively. The numerical prefactor was determined to be $\beta_5 = 0.7$.

Our arrest model for inertial droplet impacts simply balances the spreading velocity with the kinetic velocity of the nonequilibrium freeze front. The inertio-viscous spreading velocity is obtained by solving Eq. (6) for the contact line velocity: $v_{cl} \sim w/t$, resulting in $v_{cl} \sim ReU(D_0/w)^5$. Assuming that droplet spreading gets arrested once the kinetic freezing front speed matches that of the contact line [12,28], we obtain the nondimensional arrested diameter

$$\frac{w_{\text{arrest}}}{D_0} \sim \beta_5 \left[\left(\frac{U}{\kappa} \right) \frac{1}{(T_f - T_l)^b} \right]^{1/5} Re^{1/5}. \quad (8)$$

Interestingly, the maximal inertial spreading of a viscous drop (in the absence of freezing) also scales with $Re^{1/5}$ [42], with our freezing-induced arrest model additionally exhibiting an inverse relation to the kinetic coefficient of undercooling and the temperature differential. Plotting all experimental data in Fig. 4, Eq. (8) successfully predicts w_{arrest} when using $\kappa = 2.8 \times 10^{-3} \text{ ms}^{-1} \text{ K}^{-2}$ and $b = 2$, when assuming that the local undercooling approaches the same temperature as the ice substrate ($T_l \approx T_s$). It is remarkable that these singular fitting values agreed with the data over a wide range of Weber numbers ($1 < We < 1000$) and for both water (Fig. 4) and hexadecane droplets (Fig. S9 [29]). Droplets that exhibited minor splashing upon impact deviated slightly from the model, presumably due to the model not accounting for the loss in volume. Interestingly, even gently deposited droplets spreading in the capillary regime exhibited a reasonable fit with Eq. (8) in Fig. 4. This is likely coincidental, as capillary spreading and its conductive cooling rate are much slower, making it unlikely that substantial undercooling could occur on an icy substrate. Alternatively, if

local undercooling is still occurring to some extent, it is possible that both arrest mechanisms [Eqs. (4) and (8)] are occurring simultaneously at roughly the same timescale.

In summary, the hydrodynamic spreading of droplets on a chilled ice substrate becomes arrested by freezing. Prior to freezing onset, spreading followed the well-known $1/2$ power law. For high Weber number impacts, spreading continued even after freezing with a $1/6$ power law, due to inertio-viscous spillage over the droplet's icy base. Spreading arrest occurred when the bulk droplet cooled down to 0°C for low Weber number impacts and when a local nonequilibrium freeze front matched the spillage velocity for high Weber number impacts. These findings indicate that, in the absence of an appreciable nucleation energy barrier, the dynamics of droplet impact and spreading are profoundly disrupted by disparate freezing phenomena, which in turn depend on the initial flow conditions.

The authors would like to acknowledge startup funds from the Department of Biomedical Engineering and Mechanics at Virginia Tech. We thank Saurabh Nath, Ranit Mukherjee, and Varun Kulkarni for fruitful discussions.

*These authors contributed equally to this work.

†Corresponding author.

boreyko@vt.edu

- [1] M. Rein, *Fluid Dyn. Res.* **12**, 61 (1993).
- [2] I. V. Roisman, R. Rioboo, and C. Tropea, *Proc. Math. Phys. Eng. Sci.* **458**, 1411 (2002).
- [3] A. L. Yarin, *Annu. Rev. Fluid Mech.* **38**, 159 (2006).
- [4] A.-L. Bianco, C. Clanet, and D. Quéré, *Phys. Rev. E* **69**, 016301 (2004).
- [5] J. C. Bird, S. Mandre, and H. A. Stone, *Phys. Rev. Lett.* **100**, 234501 (2008).
- [6] L. Courbin, J. C. Bird, M. Reyssat, and H. A. Stone, *J. Phys. Condens. Matter* **21**, 464127 (2009).
- [7] P. G. de Gennes, *Capillarity and Wetting Phenomena: Drops, Bubbles, Pearls, Waves* (Springer Science & Business Media, New York, 2013).
- [8] L. H. Tanner, *J. Phys. D* **12**, 1473 (1979).
- [9] S. L. Cormier, J. D. McGraw, T. Salez, E. Raphaël, and K. Dalnoki-Veress, *Phys. Rev. Lett.* **109**, 154501 (2012).
- [10] J. Lee, N. Laan, K. de Bruin, G. Skantzaris, N. Shahidzadeh, D. Derome, J. Carmeliet, and D. Bonn, *J. Fluid Mech.* **786**, R4 (2016).
- [11] M. Pasandideh-Fard, R. Bhola, S. Chandra, and J. Mostaghimi, *Int. J. Heat Mass Transfer* **41**, 2929 (1998).
- [12] M. V. Snielen, R. de Ruiter, R. B. J. Koldeweij, D. Lohse, J. H. Snoeijer, and H. Gelderblom, *J. Fluid Mech.* **883**, A32 (2020).
- [13] V. Thiévenaz, T. Séon, and C. Josserand, *J. Fluid Mech.* **874**, 756 (2019).
- [14] P. Kant, R. B. J. Koldeweij, K. Harth, M. A. J. van Limbeek, and D. Lohse, *Proc. Natl. Acad. Sci. U.S.A.* **117**, 2788 (2020).

- [15] M. Schremp, I. V. Roisman, and C. Tropea, *J. Fluid Mech.* **835**, 1087 (2018).
- [16] L. Mishchenko, B. Hatton, V. Bahadur, J. A. Taylor, T. Krupenkin, and J. Aizenberg, *ACS Nano* **4**, 7699 (2010).
- [17] T. Maitra, C. Antonini, M. K. Tiwari, A. Mularczyk, Z. Imeri, P. Schoch, and D. Poulikakos, *Langmuir* **30**, 10855 (2014).
- [18] D. Song, Y. Jiang, T. Chou, K. Asawa, and C. Choi, *Langmuir* **36**, 11245 (2020).
- [19] Z. Jin, H. Zhang, and Z. Yang, *Int. J. Heat Mass Transfer* **109**, 716 (2017).
- [20] Z. Jin, X. Cheng, and Z. Yang, *Int. J. Heat Mass Transfer* **107**, 906 (2017).
- [21] R. de Ruiter, P. Colinnet, P. Brunet, J. H. Snoeijer, and H. Gelderblom, *Phys. Rev. Fluids* **2**, 043602 (2017).
- [22] V. Thiévenaz, T. Séon, and C. Josserand, *Europhys. Lett.* **132**, 24002 (2020).
- [23] S. Schiaffino and A. A. Sonin, *Phys. Fluids* **9**, 2217 (1997).
- [24] S. Schiaffino and A. A. Sonin, *Phys. Fluids* **9**, 2227 (1997).
- [25] S. D. Aziz and S. Chandra, *Int. J. Heat Mass Transfer* **43**, 2841 (2000).
- [26] R. Bhole and S. Chandra, *J. Mater. Sci.* **34**, 4883 (1999).
- [27] F. Tavakoli, S. H. Davis, and H. P. Kavehpour, *Langmuir* **30**, 10151 (2014).
- [28] R. de Ruiter, P. Colinnet, P. Brunet, J. H. Snoeijer, and H. Gelderblom, *Phys. Rev. Fluids* **2**, 043602 (2017).
- [29] See Supplemental Material at <http://link.aps.org/supplemental/10.1103/PhysRevLett.129.074502> for details on the experimental setup, nine supporting figures, and one supporting video.
- [30] L. Gordillo, T.-P. Sun, and X. Cheng, *J. Fluid Mech.* **840**, 190 (2018).
- [31] K. G. Winkels, J. H. Weijers, A. Eddi, and J. H. Snoeijer, *Phys. Rev. E* **85**, 055301(R) (2012).
- [32] J. Paulsen, J. Burton, S. Nagel, S. Appathurai, M. Harris, and O. Basaran, *Proc. Natl. Acad. Sci. U.S.A.* **109**, 6857 (2012).
- [33] S. Mitra and S. Mitra, *Langmuir* **32**, 8843 (2016).
- [34] L. Opfer, I. V. Roisman, J. Venzmer, M. Klostermann, and C. Tropea, *Phys. Rev. E* **89**, 013023 (2014).
- [35] I. V. Roisman, E. Berberović, and C. Tropea, *Phys. Fluids* **21**, 052103 (2009).
- [36] J. C. Bird, S. Mandre, and H. A. Stone, *Phys. Rev. Lett.* **100**, 234501 (2008).
- [37] G. A. Colligan and B. J. Bayles, *Acta Metall.* **10**, 895 (1962).
- [38] R. K. Shukla, V. Patel, and A. Kumar, *J. Therm. Spray Technol.* **27**, 269 (2018).
- [39] Y. Lahmar-Mebdoua, A. Vardelle, P. Fauchais, and D. Gobin, *Int. J. Therm. Sci.* **49**, 522 (2010).
- [40] M. Bussmann, J. Mostaghimi, and S. Chandra, *Phys. Fluids* **11**, 1406 (1999).
- [41] D. Singh and A. Kumar, *Therm. Sci. Eng. Prog.* **20**, 100722 (2020).
- [42] D. R. C. Clanet, C. Beguin, and D. Quéré, *J. Fluid Mech.* **517**, 199 (2004).

Correction: Equation (1) contained an error that also required modifications to text between Eqs. (3) and (4), and a minor mistake was detected in the phrase before Eq. (6). These errors have been set right. In addition, two mistakes regarding proof change requests were made by the production staff. (1) In the fifth paragraph, the symbol for the quantity for the density of water was misset. (2) In the seventh paragraph, first sentence, the production team removed the wrong phrase. These errors have also been set right.